

Keck spectroscopic survey of strongly lensed galaxies in Abell 1703: further evidence for a relaxed, unimodal cluster

Johan Richard^{1,2,*}, Liuyi Pei², Marceau Limousin^{3,4}, Eric Jullo⁵, and Jean-Paul Kneib⁵

¹ Durham University, Physics and Astronomy Department, South Road, Durham DH3 1LE, UK, Johan.Richard@durham.ac.uk

² Caltech Astronomy, MC105-24, Pasadena, CA 91125, USA

³ Laboratoire d'Astrophysique de Toulouse-Tarbes, Université de Toulouse, CNRS, 57 avenue d'Azereix, 65000 Tarbes, France

⁴ Dark Cosmology Centre, Niels Bohr Institute, University of Copenhagen, Juliane Marie Vej 30, 2100 Copenhagen, Denmark

⁵ Laboratoire d'Astrophysique de Marseille, OAMP, CNRS-Université Aix-Marseille, 38 rue Frédéric Joliot-Curie, 13388 Marseille Cedex 13, France

Received ; accepted

ABSTRACT

Context. Strong gravitational lensing is a unique tool to model with great accuracy the inner mass distribution of massive galaxy clusters. In particular, clusters with large Einstein radii provide a wealth of multiply imaged systems in the cluster core. Measuring the redshift of these multiple images provide strong constraints to determine precisely the shape of the central dark matter profile.

Aims. This paper presents a spectroscopic survey of strongly lensed galaxies in the massive cluster lens Abell 1703, displaying a large Einstein radius ($28''$ at $z = 2.8$) and a high number of known strongly-lensed systems including a central *ring-like* configuration.

Methods. We used the LRIS spectrograph on Keck to target multiple images and lensed galaxy candidates, and use the measured spectroscopic redshifts to constrain the mass distribution of the cluster using a parametric model.

Results. The spectroscopic data enable us to measure accurate redshifts for 7 sources at $z > 2$, in good agreement with their photometric redshifts, and to update the identification of multiply imaged systems by discovering 3 new systems and identifying a radial counter image. We also report the discovery of a remarkably bright $\sim 3.6 L^* i$ -band dropout at $z = 5.827$ in our mask which is only moderately magnified by the cluster ($\mu \sim 3.0 \pm 0.08$). The improved parametric mass model, including 16 multiple systems with 10 spectroscopic redshifts, further constrain the smooth cluster-scale mass distribution with a generalized NFW profile of best-fit logarithmic slope $\alpha = 0.92 \pm 0.04$, concentration $c_{200} = 4.72 \pm 0.40$ and scale radius $r_s = 476 \pm 45$ kpc. The overall RMS in the image plane is $1.3''$.

Conclusions. Using our strong-lensing model, we predict a shear signal on larger scale which is consistent with weak-lensing measurements inferred from Subaru data out to $4 \text{ Mpc } h^{-1}$. Together with the fact that the strong-lensing modeling requires a single dark matter clump, this argues for Abell 1703 to be a relaxed, unimodal cluster. This unique cluster could be probed further using deep X-ray, SZ and dynamics analysis, allowing a detailed study of the physics in a relaxed cluster.

Key words. Galaxies : high-redshift – Galaxies : distances and redshift – Gravitational lensing – Galaxies : clusters: individual: Abell 1703

1. Introduction

Massive galaxy clusters with large Einstein radii ($R_E \gtrsim 20''$) offer a wealth of information about their central mass distribution, as they display large number of multiple images in their strong lensing regions. The most striking case is the cluster Abell 1689, with $R_E \sim 50''$ (Broadhurst et al. 2005; Limousin et al. 2007), which holds the largest number of strong lensing constraints in a single field. This gives a great opportunity to map inner mass profiles to a high precision level. Parametric cluster-lens mass models have been widely used (Kneib et al. 1996; Smith et al. 2005; Richard et al. 2007), but to reach a high accuracy on the mass model and their fiducial parameters accurate redshift information are necessary. Indeed, one redshift of multiple image enables to estimate the absolute total mass within the Einstein radius. Adding many more redshifts allow to measure the full central mass profile accurately. Even though photometric redshifts offer an acceptable level of precision for such modeling (Broadhurst et al. 2005; Bradač et al. 2008), spectroscopic red-

shifts are the most reliable way to confirm the identifications and find new multiply-imaged systems. Lowering down the redshift error on the multiple systems with spectroscopy has another great interest, as one can use strong-lensing to constrain the cosmological parameters w and Ω_m based on pure geometrical considerations (Link & Pierce 1998; Golse et al. 2002).

On the theoretical side, Broadhurst & Barkana (2008) recently compared the measured lensing parameters for a sample of clusters with large R_E , with predictions from the standard Λ CDM cosmology, and report a $4\text{-}\sigma$ discrepancy in the presence of such large R_E for the corresponding virial mass. However this result, based on a sample of massive haloes derived from the Millennium simulation, might not be representative of an all-sky survey for such extreme clusters. As shown in Oguri & Blandford (2008), who investigated full-sky Monte-Carlo realizations of massive clusters, the population of clusters with large Einstein radii is scarce, and largely biased towards alignments of their triaxial dark-matter haloes along the line of sight. They find that Einstein radii as large as $50''$ can be found in the whole sky with a WMAP5 cosmology, which releases any disagreement between the presence of large R_E and Λ -CDM.

Send offprint requests to: J. Richard

* Marie-Curie fellow

Among the clusters with large R_E , we have started to study the cluster Abell 1703 in Limousin et al. (2008), hereafter L08, for the purpose of determining its mass distribution. In this previous work, we have identified 13 systems forming highly-magnified multiple images, including a central ring. Based on the spectroscopic redshift of this central feature and photometric redshifts for the remaining images, all the lensing systems have shown to be well reproduced by a single NFW (Navarro et al. 1997) profile for the dark matter, making Abell 1703 somewhat *simpler* compared to bimodal lensing clusters (e.g. Elíasdóttir et al. 2007 for Abell 2218, Richard et al. 2007 for Abell 68, Verdugo et al. 2007 for MS2053). We therefore decided to use it as a more reliable probe for comparing the results of strong and weak-lensing measurements in clusters with large Einstein radii from Broadhurst et al. (2008).

We present in this paper results from a spectroscopic survey conducted at Keck using the LRIS instrument, aiming at confirming the photometric redshifts, multiply images identification, and precisely constraining the mass distribution in Abell 1703. We obtained new spectroscopic redshift measurements for nearly all the systems identified by L08 (10 out of 13), in good agreement with their corresponding photometric redshifts. We also report of an exceptionally bright *i*-band dropout at $z \sim 6$, forming a magnified single image close to the region of multiple images. We have further identified three new systems of multiple images and constrained the lensing model, as well as compared the weak-lensing extrapolation of our model to the recently measured weak-lensing profile of Broadhurst et al. (2008).

We present in Section 2 the observations and data reduction of the spectroscopic data. Section 3 gives the redshift measurements, spectra and the main results from the mass modeling. We discuss these results in Section 4. Throughout the paper, we used a standard Λ -CDM model with $\Omega_m = 0.3$, $\Omega_\Lambda = 0.7$ and $H_0 = 70$ km s⁻¹ Mpc⁻¹, whenever necessary. In this cosmology, a physical distance of 4.244 kpc at the redshift $z = 0.28$ of the cluster corresponds to 1'' on the sky. All magnitudes are quoted in the AB system.

2. Observations

2.1. Imaging and photometric redshifts

The current study is based on the same imaging data described in L08, based on Hubble Space Telescope and Subaru observations of Abell 1703 covering broad-band filters from *B* to *H*. These images were previously used to derive photometric redshifts with the software Hyperz (Bolzonella et al. 2000). We briefly summarize the characteristic parameters, central wavelength and depth, of these images in Table 1.

2.2. Keck spectroscopy

We have used the Low Resolution Imager and Spectrograph (LRIS, Oke et al. 1995) on the Keck telescope to perform multi-slit observations of the Abell 1703 cluster field. We designed a multi-slit mask containing 32 slits of 1.0'' width to include as many of the multiple systems previously identified in L08 as possible, with a few tilted slits following the geometry of long arcs (Fig. 1). In the case of fainter or less reliable identifications, independent images of the same system were observed in separate slits. Additional slits in the mask included new multiple systems candidates, cluster members and background galaxies as estimated through their photometric redshifts.

The LRIS instrument was set up with a 6800 Å dichroic isolating the blue arm, with a 300 lines/mm grism blazed at 5000 Å, from the red arm, with a 600 lines/mm grating blazed at 7500 Å. This ensures a high throughput over the wavelength range 3500 to 9500 Å and good spectral resolution in the red to resolve sky-lines as well as [OII] emission line doublets in the redshift range 0.85 – 1.40. This instrument setup is also well-matched with the photometric redshift estimates of the targetted sources. We obtained 2 hours of exposure time on 2008 May 10 in photometric conditions and very good seeing (0.7'').

2.3. Data reduction and redshift measurements

Data reduction of the spectra was performed using the Python version of the Kelson (2003) reduction scripts, which offer the advantage of processing the images in their distorted framework. This helps to reduce noise correlations, in particular for the case of tilted slits. We performed standard reduction steps for bias removal, flat-field correction, wavelength calibration, sky subtraction and cosmic-ray rejection, and used observations of the standard star BD+33-2642 obtained on the same night to derive the flux calibration.

Close-ups on the targets and extracted spectra are presented in Fig. 2 and 3. We measured the redshift for 33 sources in the entire LRIS mask. The majority of the spectra show clear Lyman- α / [OII] in the blue / red part of the spectrum, in emission or in absorption. Either the resolved doublet (for [OII]) or additional ultraviolet absorption lines (for Lyman- α) confirm this interpretation. In two multiple systems (10/11 and 16), we observed these images in multiple slits: redshift measurements were obtained by identifying significant absorption lines after stacking the relevant exposures. For each spectrum, the average redshift value is obtained from the peaks of the main spectral features identified, while the corresponding error is taken from the spectral dispersion. Additional uncertainties generated by the accuracy of the relative and absolute wavelength calibrations, of about 1.1 and 1.5 Å, respectively, were quadratically added to yield the final redshift errors. A confidence class z_{class} , ranging from 1 to 4, was assigned to each measurement according to the prescription of Le Fevre et al. (1995): this corresponds to a probability level for a correct identification of 50%, 75%, 95%, and 100%, respectively. A specific value of 9 is used when only a single secure spectral feature is seen in emission.

Table 2 summarizes the redshift measurements z_{spec} , confidence class z_{class} and the spectral features used to derive the redshift for all objects detected in the LRIS mask, including those additional targets serendipitously falling into the slits. For the majority of sources located within the ACS field of view, we report in the same table the corresponding photometric redshift z_{phot} . We find a good agreement between individual z_{spec} and z_{phot} values, with a typical error $< |z_{phot} - z_{spec}| \geq 0.15$ or $< \frac{|z_{phot} - z_{spec}|}{1 + z_{spec}} \geq 0.047$, and no *catastrophic* measurements. This strong consistency is mainly owing to the use of space-based images of very similar PSF size, together with ground based near-infrared images obtained with MOIRCS in excellent seeing conditions (0.4'').

3. Results

3.1. Multiple images redshifts and identifications

Our spectroscopic data enabled to measure the redshifts for 8 of the 11 known multiply-imaged sources from the previous work presented in L08:

- System 1 at $z = 0.8889$ forms a very highly magnified ring-shaped configuration with 4 images close to the BCG and a less-magnified 5th image to the South-West. Although its redshift was previously derived in L08, we obtained a new spectrum with the same mask in much better conditions.
- System 3 at $z = 3.277$ is located to the North of the BCG, with 3 images: 2 bright merging images and a fainter counter-image to the West.
- Systems 4/5 at $z = 1.9082$ are two individual regions identified in the same source which forms a cusp configuration of 3 images.
- System 6 at $z = 2.360$ is a similar configuration as Systems 4/5, but closer to the center of the cluster.
- System 7 at $z = 2.983$ is again a cusp configuration like Systems 4/5, but further from the center of the cluster.
- Systems 10/11 at $z = 2.627$ are two individual regions identified in the giant tangential arc at the South-East of the BCG. A fainter counter-image is located to the West. The new mass model presented here enable us to associate the radial feature reported in L08, very close to the BCG (next to the ring configuration of System 1) to be a 4th image (10.4) associated with this arc.
- System 15 at $z = 2.355$ is a typical *Einstein-cross* configuration of 4 images surrounding the BCG. We note that systems 6 ($z = 2.360$) and 15 ($z = 2.355$) have similar redshifts and are therefore very close to one another in the source plane, with a projected separation of 67 ± 6 kpc.
- System 16 at $z = 2.810$ is another *Einstein-cross* configuration located at a slightly higher redshift, but found very close to System 15 in the image plane due to projection effects.

Additional sources 20 and 21, which were included in the mask as a possible new multiple system, show a very similar spectroscopic redshift $z = 1.279$ with [OII] doublet of emission lines. However, they are located too far from the center of the cluster to be multiply imaged at this redshift.

Apart from system 1, the other systems are located in the redshift range $1.9 < z < 3.3$. Using the new spectroscopic redshifts into the mass model (see Sect. 3.3), we have computed the predicted region of multiple images for a redshift $z = 6$ (delimited with a dashed line in Fig. 1). As we expect all the multiple images present in the HST optical bands to lie within this region, we use it to update our systematic search for multiple images based on the photometric redshifts catalog. We find three additional systems complementing the list presented in L08, and report the corresponding positions and photometric redshifts in Table 3:

- System 12 is again a typical cusp configuration of 3 images located to the North, and "following" the nearby Systems 4/5, 7, 8 and 9.
- System 13 and 14 are two further *Einstein-cross* configurations of 4 images surrounding the BCG. System 14 is located near the Systems 15 and 16 in the image plane, while System 13 is closer to the cluster center.

3.2. Spectroscopy of a remarkably bright *i*-dropout

One of the sources in the LRIS mask, identified as 23 in the spectroscopic catalog (Table 2), has been selected for its very red $i - z = 2.9 \pm 0.3$ color and bright $z = 24.30 \pm 0.07$, while being undetected blueward of the *i* band in the other deep ACS images. The NICMOS and MOIRCS photometry $J = 23.93 \pm 0.07$ and $H = 23.75 \pm 0.10$ further constrain its spectral energy distribution to be compatible with a photometric redshift $z_{phot} = 6.0 \pm 0.42$ (Figure 4, top and middle panels), and the $i - z$ color make it a very strong *i*-dropout photometric candidate according to the Bouwens et al. (2006) selection criterion.

The LRIS spectrum for this object covers the wavelength range 3800-9230 Å, corresponding to $2.12 < z < 6.59$ for Lyman- α . We detect a 5σ -significant emission line at $\lambda = 8301$ Å (Figure 4, lower panel), with an integrated flux $f = 2.5 \pm 0.4 \times 10^{-17}$ ergs s⁻¹ cm⁻². This line is slightly resolved in the spectral direction, with a possibly asymmetric profile. It is therefore likely to be Lyman- α at a redshift $z = 5.827$, quite compatible with the photometric redshift prediction.

After correcting for the magnification factor $\mu = 3.0 \pm 0.08$ (1.2 magnitudes), this source is both magnified and intrinsically bright ($H_{unlensed} = 24.9$), as there are only 9 of such sources at $z \sim 6$ brighter than $z = 25.5$ AB found in the UDF, HUDF and GOODS fields (Bouwens et al. 2006). This object is similar in redshift and intrinsic magnitude to the spectroscopically confirmed *i*-dropouts by Stanway et al. (2004) at $z = 5.78$ and $z = 5.83$, or the slightly magnified object at $z = 5.515$ found in the cluster RDCS1252.9-292 (Dow-Hygelund et al. 2005). Based on the latest constraints of the luminosity function at $z \sim 6$ (Bouwens et al. 2008), the unlensed magnitude corresponds to an $3.6 L^*$ galaxy. We also note that the very red $i - z = 2.9$ color is much redder than for any of the 9 dropouts with $z < 25.5$ from Bouwens et al. (2006), detected in both the *i* and *z* bands, and where the reddest color was found to be $i - z = 2.4$.

3.3. Strong Lensing

3.3.1. Modeling method

Our starting point in modeling of the dark matter distribution in Abell 1703 is the mass model presented in details by L08, where we used the LENSTOOL software (Jullo et al. 2007) to constrain a parametric mass model with the identified multiple systems.

The contribution of the stellar mass from the central galaxy is parametrized by a Pseudo Isothermal Elliptical Mass Distribution (PIEMD) using the profile derived from the photometry. The PIEMD profile, which has been widely used for both cluster-scale (Smith et al. 2005) and galaxy-scale (Natarajan et al. 1998) haloes, assumes each dark matter clump can be parametrized by a central position, ellipticity e , position angle θ , central velocity dispersion σ_0 , and two characteristic radii: a core and a cut radius. The total mass is proportional to $r_{cut} \sigma_0^2$. The cluster-scale dark-matter component is modeled with a generalized NFW (hereafter gNFW) profile (Zhao 1996) including a central logarithmic slope α :

$$\rho(r) = \frac{\rho_c \delta_c}{(r/r_s)^\alpha (1 + (r/r_s))^{(3-\alpha)}} \quad (1)$$

where r_s is a scale radius, ρ_c the critical density and δ_c is related to the value of the concentration parameter c_{200} through the relation:

$$\delta_c = \frac{200}{3} \frac{c_{200}^3}{\ln(1 + c_{200}) - c_{200}/(1 + c_{200})} \quad (2)$$

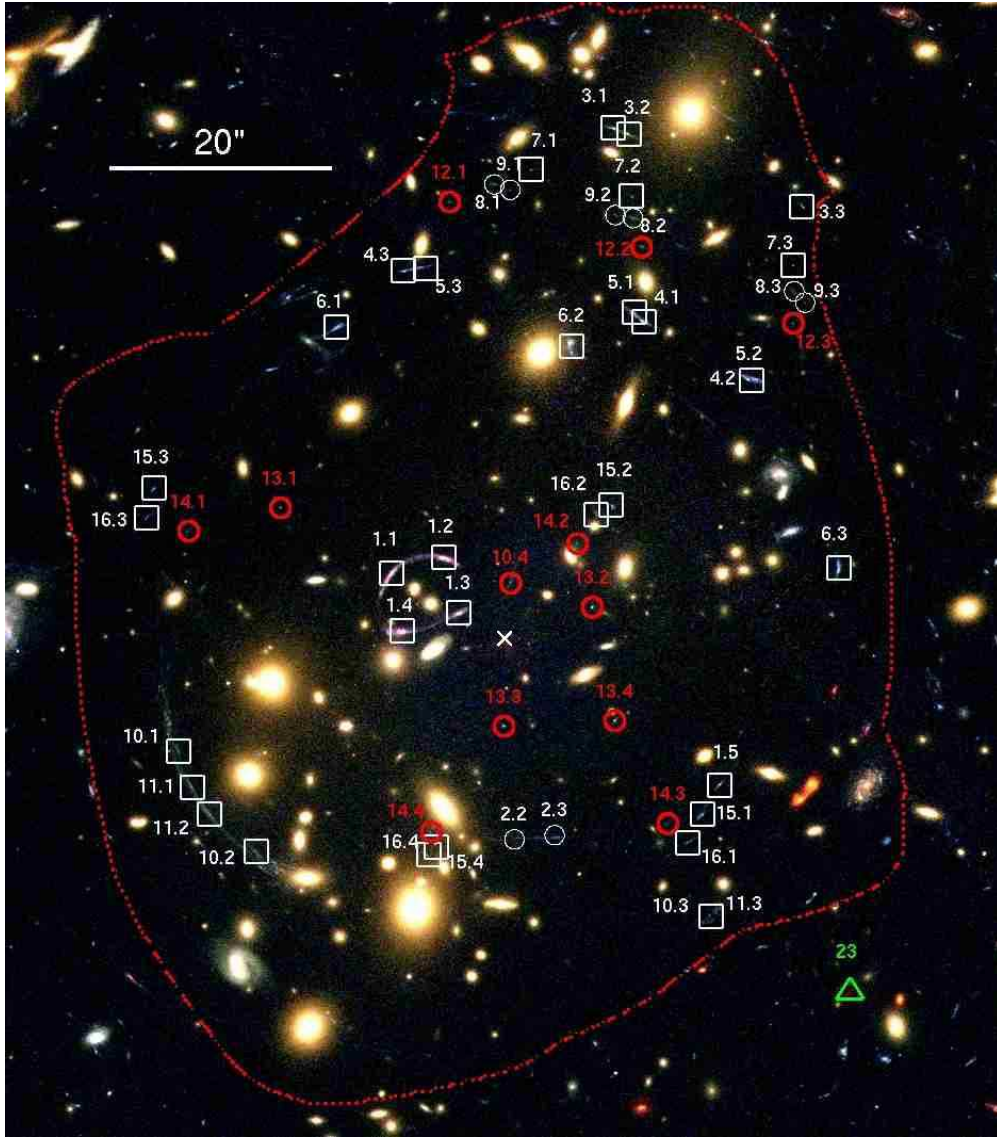


Fig. 1. BVZ ACS color image of Abell 1703, showing the location of all the multiply-imaged systems included in this study. The white cross at the center of the image marks the location of the brightest cluster galaxy, which has been subtracted for clarity. The dashed line outlines the limit of the region where we expect multiple images up to $z = 6$. The systems presented in L08 are shown in white, and the new systems presented in this work are shown in red. Squares identify the multiple images with spectroscopic redshifts. The green triangle located to the lower right marks the location of the i -band dropout presented in Section 3.2.

Individual cluster galaxies were added as small-scale PIEMD perturbors based on their photometry and shape parameters, using empirical scaling relations between their dynamical parameters (central velocity dispersion and scale radius) and their luminosity, assuming the Faber & Jackson (1976) relation and a constant mass-to-light ratio for each galaxy (see Covone et al. 2006 for more details). The same parameters of one particular cluster galaxy to the north (852) were optimized individually to reproduce the configuration of the surrounding systems 3, 7, 8, 9 and 12.

We replaced the photometric redshifts kept as free parameters in L08 by their spectroscopic equivalents for the 7 relevant sources (9 systems). The precision of the new model, which uses the same parametrization as L08, can be estimated using the

RMS of the location of multiple images in the image plane, defined as:

$$\sigma_i = \sqrt{\sum_{j,k} (x_{\text{obs}_{j,k}} - x_{\text{pred}_{j,k}})^2 + (y_{\text{obs}_{j,k}} - y_{\text{pred}_{j,k}})^2} \quad (3)$$

where $(x_{\text{obs}_{j,k}}, y_{\text{obs}_{j,k}})$ and $(x_{\text{pred}_{j,k}}, y_{\text{pred}_{j,k}})$ are the observed and predicted location of image j in system k , respectively. Using the exact same parametrization, we find a value of $\sigma_i = 1.3''$ similar to the result obtained in L08 ($1.4''$). This precision is typical of strong lensing works using a similar number of multiples images (Richard et al. 2007; Elíasdóttir et al. 2007), and smaller by a factor of ~ 2 from the one obtained for Abell 1689 ($2.87''$, Limousin et al. 2007). We summarize the best fit parameters of the new model in Table 4.

Fig. 2. BVI ACS color image close-up on individual $z > 0.5$ sources in the LRIS mask with the location of the slit, and corresponding extracted spectra. The i -band dropout (23, see Sect. 3.2) is presented separately in Fig. 4.

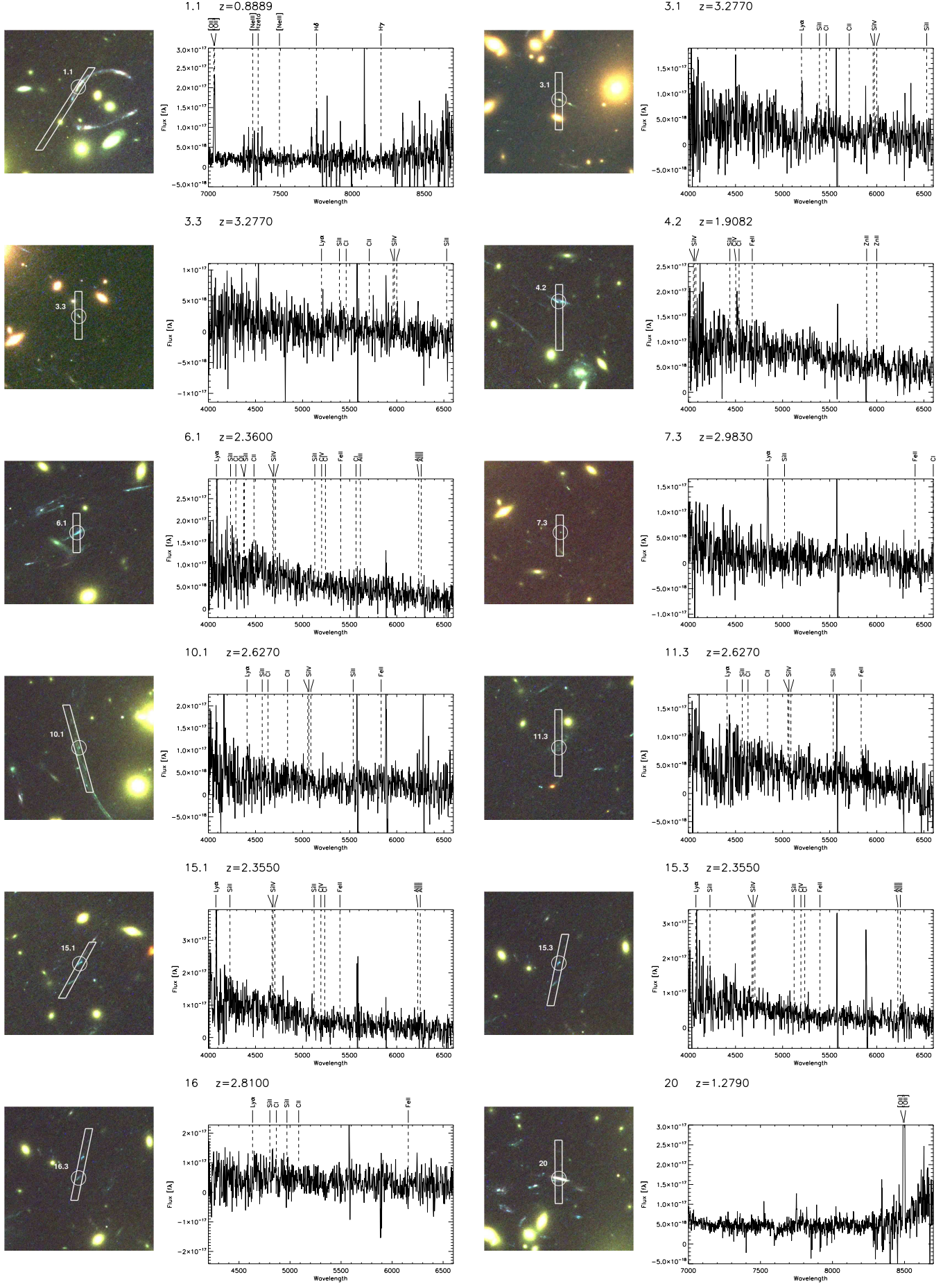
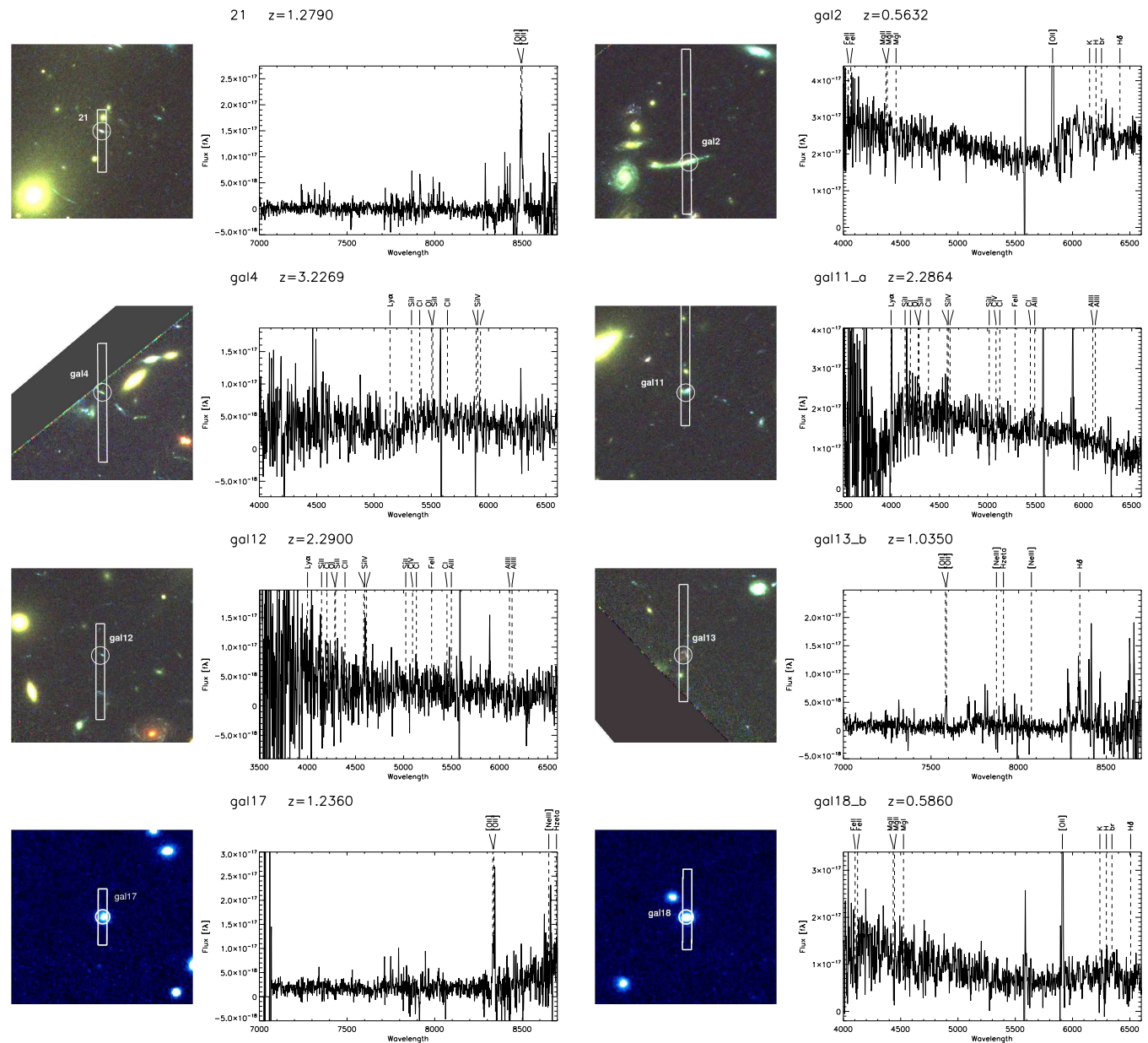


Fig. 3. Continuation of fig. 2



3.3.2. Redshift predictions and magnifications

We used the MCMC realizations to estimate the redshift and associated error for each of the new multiple systems 12, 13 and 14. These values are reported in Table 3. We also computed the magnification factors μ and associated error for every source in our LRIS mask (Table 2) as well as the other multiple systems (Table 3). The magnification factors ranges from a few percent for single images to about 80 for the source 1.1.

3.3.3. Weak-lensing predictions

Our mass model, solely based on strong lensing constraints out to $50''$ (the region of multiple images), can be used to predict the tangential *shear* induced on background galaxies up to larger scales. The main observable with weak-lensing is the *reduced shear* $g = \gamma/(1 - \kappa)$ where γ is the gravitational shear and κ the convergence. In order to compare our predictions with weak-

lensing observations of Abell 1703 with Subaru described by Broadhurst et al. (2008), we adopt the definition of the *tangential reduced shear* g_+ from Umetsu & Broadhurst (2008), i.e. the projection of the shear perpendicularly to the direction of the cluster center (see also Medezinski et al. 2007).

Using the MCMC realizations, we determine predictions for g^+ and its associated $3\text{-}\sigma$ error as a function of angular distance r from the center of the mass distribution, assuming a distribution of background sources at a fixed redshift $z_s = 1.2$ corresponding to the mean of the redshift distribution of sources in the observations from Broadhurst et al. (2008). Figure 5 presents these estimations against their weak-lensing measurements over the same range of r . We find that our strong-lensing model represents a very good fit to the weak-lensing datapoints up to $4 \text{ Mpc} h^{-1}$, with a χ^2 of $4.1 / 7 = 0.58$, even after extrapolating our mass model to a radial distance $20\times$ larger than the region of strong lensing constraints. This argues again for the overall sim-

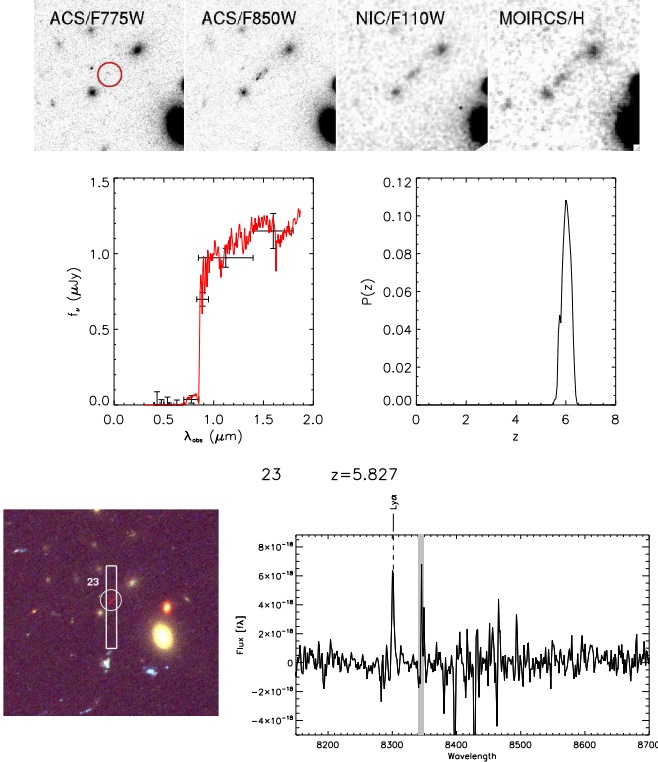


Fig. 4. A bright *i*-dropout found in the field of Abell 1703. The top panel shows the individual detections in the ACS, NICMOS and MOIRCS image. The object is resolved and elongated along the shear direction, with an angular size $0.45''$. Middle panels: best fit of the spectral energy distribution with the photometric redshift software (left), and corresponding redshift probability distribution (right). Bottom panels: VIZ ACS color image with the location of the LRIS slit (left), and close-up on the extracted spectrum where we detected an emission line at 8301 \AA (right). The grey region highlights the location of a bright OH skyline.

plicity of the cluster, with a single NFW profile providing a good fit both for the strong-lensing and weak-lensing measurements.

3.3.4. Ellipticity of the mass distribution and Einstein radius

From the best fit geometrical parameters found during the optimization of the mass model (Table 4), we notice a good agreement between the values for the ellipticity and position angle of the large scale gNFW profile ($e_{\text{NFW}} = 0.23$, $\theta_{\text{NFW}} = 63.9$ degrees) and the same parameters of the cD galaxy ($e_{\text{cD}} = 0.19$, $\theta_{\text{cD}} = 52$ degrees) as measured with SExtractor¹. This is not really surprising, as this correlation has previously been reported both in strong-lensing analysis (e.g. Gavazzi et al. 2003 in MS2137), X-ray observations (Hashimoto et al. 2008) as well as numerical works (Dubinski 1998; Faltenbacher et al. 2005).

More generally, the total mass distribution of dark matter is the sum of this gNFW component and the various PIEMD profiles associated with the cluster galaxies, and the global ellipticity e_{mass} may have a different value. We use the convergence map κ (which shares an identical geometry with the mass distribution) to measure this ellipticity e_{mass} *a posteriori* by fitting elliptical

¹ We use here the definition $e = 1 - b/a$ of the ellipticity, where a and b are the semi-major and semi-minor axis of the ellipse, respectively. The value of e_{NFW} given in L08 had an error in its definition and we update it to the correct one.

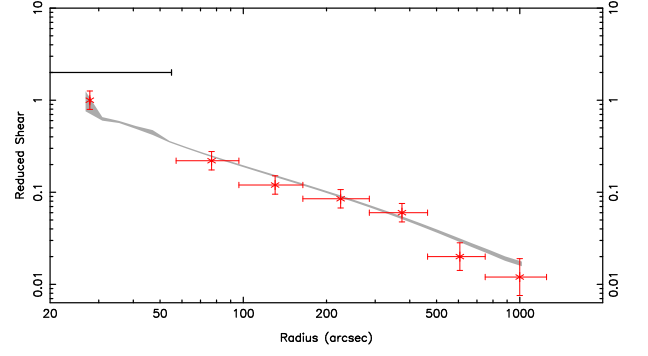


Fig. 5. Tangential reduced shear g_+ predicted with the strong lensing model based on constraints in the central region (black error bar on top). The mean value and 3σ error is presented as a function of radius in the grey-filled region. We overplot the datapoints obtained by Broadhurst et al. (2008) in their weak-lensing measurements with Subaru. Extrapolation of our strong lensing model forms a very good fit to these observations upto $r = 1000 \text{ arcsec}$, or $4 \text{ Mpc } h^{-1}$.

contours with the IRAF routine ellipse. We keep the center of the ellipses fixed at the peak of the mass map and let the ellipticity $e_{\text{mass}}(a)$ and position angle $\theta(a)$ vary as free parameters with the semi major axis a . In the central region ($a < 15''$), we find a best fit value $e_{\text{mass}} \sim 0.23$ (Fig. 6, in blue) dominated by the geometry of the cD and the gNFW profile. At larger distances $e_{\text{mass}}(a)$ increases to reach a maximum of 0.4 at $a \sim 40''$ (Fig. 6, in green), due to an alignment of bright galaxies (as seen in projection) to the north-west and the south-east, therefore along a similar direction as θ_{NFW} . These galaxies contribute to increasing the value of e_{mass} compared to e_{NFW} , this effect being significant on the mass distribution up to the edge of the ACS field of view. The same ellipticity is seen on the weak-lensing reconstructions performed by Broadhurst et al. (2008).

We also compute the *effective* Einstein Radius R_E , defined as the radius r from the center of the cluster (located at the peak of the mass distribution) at which $\bar{\kappa}(r < R_E) = 1$ (Broadhurst & Barkana 2008). We measure the value and error on R_E for the redshift $z = 2.627$ of the giant tangential arc (formed with the systems 10 and 11), using the different MCMC realizations. We find $R_E = 28.0 \pm 0.25 \text{ arcsec}$, a value smaller than one would measure based on the simple distance of the giant arc, due to the ellipticity of the mass distribution (Fig. 6). This value is close but smaller than the estimate of $33''$ given by Broadhurst & Barkana (2008). Using their estimates of the cumulative probability distribution $P(> R_E)$ for an agreement between this R_E and the Millennium simulation ΛCDM , we find a higher probability $P=20\%$ (instead of 7.9%) of agreement, making Abell 1703 less discrepant than the other mentioned clusters (Abell 1689, CL0024 and RXJ1347). As mentioned earlier, considering the inherent biases of this cluster sample towards large concentration values, there is a good agreement of the Einstein radius with predictions from the simulations.

4. Abell 1703: a relaxed, unimodal cluster ?

Our strong lensing analysis using a simple NFW component for the large scale dark matter distribution, after individual treatment of the central cD galaxy and small scale mass distributions associated with the galaxy substructure in the cluster, is able to reproduce the large number of multiple images identified in Abell 1703. Even if the overall RMS in the predicted location of the

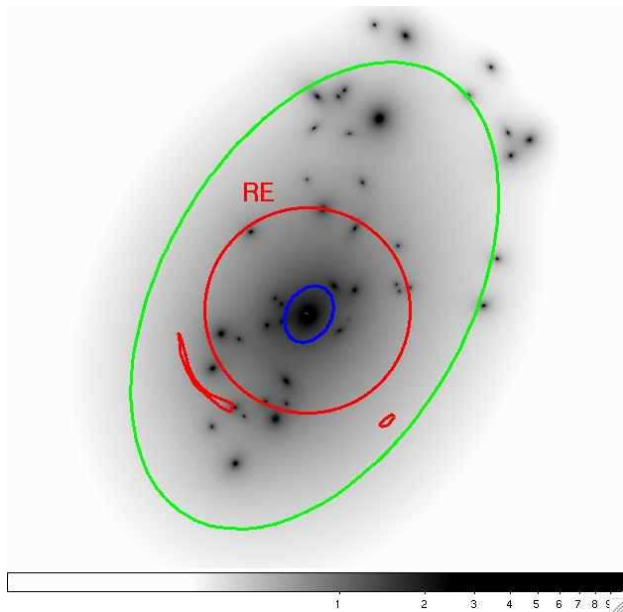


Fig. 6. Convergence map distribution κ for a source at $z = 2.627$, the redshift of the giant tangential arc (systems 10 and 11, located in red). By averaging this map inside increasing apertures, we measure the corresponding *effective Einstein radius* R_E , slightly shorter than the distance to the giant arc due to the overall ellipticity of the mass distribution. The blue and green ellipses show the best-fit ellipses found on the overall mass distribution, with an increasing ellipticity when moving from small to large radii (see Sect. 3.3.4 for details).

multiple images ($1.3''$) is still quite larger than the precision in astrometric measurements with HST (typically $0.1''$), we find no systematics as a function of the location of the multiples, that would argue for the need of secondary dark matter clumps. This was the case in the clusters Abell 2218 (Elíasdóttir et al. 2007) and Abell 68 (Richard et al. 2007) which show a strong evidence for *bimodality*.

Furthermore, adding new spectroscopic measurements on 7 multiple sources has removed an identical number of free parameters (i.e., the redshifts of the sources) from the analysis presented in L08. However, we found no significant increase in the overall RMS of the multiple images compared to this previous work, under the same assumptions. In addition, the strongest variations in the best fit parameters compared with the previous values presented in L08 are found for the gNFW profile, but both results are compatible within the 3σ confidence level. The remaining scatter in the positions of multiple images is very likely due to small-scale substructure in the dark matter distribution, which is not included here apart from the visible cluster galaxies. One way to increase the complexity of this model would be to estimate small-scale deviations from the smooth mass distribution, using adaptive-grid based models (Jullo et al. 2009, submitted).

Finally, the best fit parameters of our strong-lensing analysis have shown to be consistent with weak-lensing measurements. Our best fit concentration parameter $c_{200} = 4.72^{+0.43}_{-0.45}$, corresponding to $c_{vir} = 5.82^{+0.53}_{-0.56}$ with the second definition based on the virial radius r_{vir} , is somewhat lower than the value derived by Broadhurst et al. (2008), $c_{vir} = 9.92^{+2.39}_{-1.63}$, but marginally compatible at 2.4σ level. Since our NFW parameters provide an overall good fit to their observations, there seems to be smaller discrepancy between our strong and their weak lensing measure-

ments, as it was the case for Abell 1689 (Broadhurst et al. 2005; Limousin et al. 2007).

Overall, we argue that these results provide further evidence for Abell 1703 to be a relaxed cluster, as was already suggested in L08. Follow-up X-ray observations of the cluster core should allow to confirm again this assumption, and also to separate the X-ray gas component from the dark matter in the mass distribution when doing the strong-lensing analysis, following the work by Bradač et al. (2008) in RXJ1347. Another independent measurement of the mass profile would be to study the dynamics of cluster galaxies up to large radii, giving another estimate of the virial radius and virial mass. Finally, we expect to find a larger sample of similar relaxed clusters from the ongoing LoCuSS survey (Zhang et al. 2008) of clusters with lower masses (as inferred from their X-ray luminosity) at $z \sim 0.2$. By pursuing the same strong lensing analysis on this broader sample, we will probe a wider distribution of Einstein radii, ellipticities and concentration parameters with less bias compared to available numerical simulations.

Acknowledgements. We acknowledge useful discussions with Masamune Oguri, Carlos Frenk and Mark Swinbank. JR acknowledges support from an European union Marie-Curie Fellowship. ML acknowledges the Agence Nationale de la Recherche for its support, project number 06-BLAN-0067. The Dark Cosmology Center is funded by the Danish National Research Foundation. We thank the Danish Centre for Scientific Computing at the University of Copenhagen for providing us generous amount of time on its supercomputing facility. JPK acknowledges the Centre National de la Recherche Scientifique for its support. The authors recognize and acknowledge the very significant cultural role and reverence that the summit of Mauna Kea has always had within the indigenous Hawaiian community. We are most fortunate to have the opportunity to conduct observations from this mountain.

References

- Bolzonella, M., Miralles, J.-M., & Pelló, R. 2000, A&A, 363, 476
- Bouwens, R. J., Illingworth, G. D., Blakeslee, J. P., & Franx, M. 2006, ApJ, 653, 53
- Bouwens, R. J., Illingworth, G. D., Franx, M., & Ford, H. 2008, ApJ, 686, 230
- Bradač, M., Schrabback, T., Erben, T., et al. 2008, ApJ, 681, 187
- Broadhurst, T., Benítez, N., Coe, D., et al. 2005, ApJ, 621, 53
- Broadhurst, T., Umetsu, K., Medezinski, E., Oguri, M., & Rephaeli, Y. 2008, ApJ, 685, L9
- Broadhurst, T. J. & Barkana, R. 2008, MNRAS, 390, 1647
- Covone, G., Kneib, J.-P., Soucail, G., et al. 2006, A&A, 456, 409
- Dow-Hygelund, C. C., Holden, B. P., Bouwens, R. J., et al. 2005, ApJ, 630, L137
- Dubinski, J. 1998, ApJ, 502, 141
- Elíasdóttir, Á., Limousin, M., Richard, J., et al. 2007, astro-ph/0710.5636
- Faber, S. M. & Jackson, R. E. 1976, ApJ, 204, 668
- Faltenbacher, A., Allgood, B., Gottlöber, S., Yepes, G., & Hoffman, Y. 2005, MNRAS, 362, 1099
- Gavazzi, R., Fort, B., Mellier, Y., Pelló, R., & Dantel-Fort, M. 2003, A&A, 403, 11
- Golse, G., Kneib, J.-P., & Soucail, G. 2002, A&A, 387, 788
- Hashimoto, Y., Henry, J. P., & Boehringer, H. 2008, MNRAS, 390, 1562
- Jullo, E., Kneib, J.-P., Limousin, M., et al. 2007, New Journal of Physics, 9, 447
- Kelson, D. D. 2003, PASP, 115, 688
- Kneib, J.-P., Ellis, R. S., Smail, I., Couch, W. J., & Sharples, R. M. 1996, ApJ, 471, 643
- Le Fevre, O., Crampton, D., Lilly, S. J., Hammer, F., & Tresse, L. 1995, ApJ, 455, 60
- Limousin, M., Richard, J., Jullo, E., et al. 2007, ApJ, 668, 643
- Limousin, M., Richard, J., Kneib, J.-P., et al. 2008, A&A, 489, 23
- Link, R. & Pierce, M. J. 1998, ApJ, 502, 63
- Medezinski, E., Broadhurst, T., Umetsu, K., et al. 2007, ApJ, 663, 717
- Natarajan, P., Kneib, J.-P., Smail, I., & Ellis, R. S. 1998, ApJ, 499, 600
- Navarro, J. F., Frenk, C. S., & White, S. D. M. 1997, ApJ, 490, 493
- Oguri, M. & Blandford, R. D. 2008, MNRAS accepted, astro-ph/0808.0192
- Oke, J. B., Cohen, J. G., Carr, M., et al. 1995, PASP, 107, 375
- Richard, J., Kneib, J.-P., Jullo, E., et al. 2007, ApJ, 662, 781
- Smith, G. P., Kneib, J.-P., Smail, I., et al. 2005, MNRAS, 359, 417
- Stanway, E. R., Bunker, A. J., McMahon, R. G., et al. 2004, ApJ, 607, 704
- Umetsu, K. & Broadhurst, T. 2008, ApJ, 684, 177

Filter	λ (μm)	Exposure Time (ksec)	Depth (AB)
ACS/F435W	0.435	7.05	26.5
ACS/F475W	0.480	5.56	27.5
ACS/F555W	0.539	5.56	27.1
ACS/F625W	0.635	8.49	27.6
ACS/F775W	0.779	11.13	27.3
ACS/F850LP	0.908	17.8	26.9
NICMOS/F110W	1.147	0.26	25.4
MOIRCS/H	1.642	18.87	25.3

Table 1. Summary of the broad-band images used for the photometry. The depth is given as the 5σ detection limit for a point source.

Verdugo, T., de Diego, J. A., & Limousin, M. 2007, ApJ, 664, 702
Zhang, Y.-Y., Finoguenov, A., Böhringer, H., et al. 2008, A&A, 482, 451
Zhao, H. 1996, MNRAS, 278, 488

ID	α (J2000.0)	δ (J2000.0)	z_{spec}	z_{phot}	F775W	μ	z_{class}	Features
1.1	198.77725	51.81934	0.8889 \pm 0.0003	0.965 $^{+0.075}_{-0.240}$	22.19 \pm 0.01	82 \pm 17	4	[OII], [NeIII], H δ , H γ
3.1	198.76696	51.83205	3.277 \pm 0.002	3.35 $^{+0.052}_{-0.034}$	22.69 \pm 0.02	23 \pm 10	4	Ly α (em), SiIV, SiII
3.3	198.75824	51.82982	3.277 \pm 0.002	3.35 $^{+0.036}_{-0.036}$	25.34 \pm 0.05	4.6 \pm 0.1	4	Ly α (em), SiIV, SiII
4.2/5.2	198.76075	51.82487	1.9082 \pm 0.004	2.25 $^{+0.216}_{-0.222}$	23.72 \pm 0.02	10.4 \pm 0.3	3	CIV, SiII, ZnII
6.1	198.77984	51.82640	2.360 \pm 0.002	2.59 $^{+0.144}_{-0.159}$	23.56 \pm 0.02	6.1 \pm 0.2	4	Ly α (em), SiIV, CIV, SiII
7.3	198.75869	51.82814	2.983 \pm 0.002	3.20 $^{+0.210}_{-0.210}$	26.81 \pm 0.10	5.6 \pm 0.1	9	Ly α (em)
10.1	198.78708	51.81424	2.627 \pm 0.004	3.10 $^{+0.324}_{-0.324}$	21.40 \pm 0.01	29.9 \pm 1.8	3	Ly α (abs), SiIV
11.3	198.76242	51.80954	2.627 \pm 0.004	2.70 $^{+0.189}_{-0.189}$	23.55 \pm 0.02	4.9 \pm 0.1	3	Ly α (abs), SiIV, SiII
15.1	198.76284	51.81246	2.355 \pm 0.002	2.44 $^{+0.171}_{-0.261}$	24.89 \pm 0.05	8.0 \pm 0.7	4	Ly α (em), CIV
15.3	198.78825	51.82173	2.355 \pm 0.002	2.60 $^{+0.130}_{-0.363}$	25.44 \pm 0.05	4.2 \pm 0.2	4	Ly α (em), SiIV, CIV
16.1/16.3	198.78851	51.82096	2.810 \pm 0.004	2.75 $^{+0.171}_{-0.165}$	25.52 \pm 0.06	4.4 \pm 0.1	3	Ly α (abs), FeII
20	198.76659	51.83626	1.279 \pm 0.0005	1.10 $^{+0.125}_{-0.126}$	21.86 \pm 0.01	4.0 \pm 0.1	4	[OII]
21	198.76000	51.83451	1.279 \pm 0.0005	1.13 $^{+0.137}_{-0.137}$	22.57 \pm 0.02	5.0 \pm 0.1	4	[OII]
23	198.75612	51.80736	5.827 \pm 0.0015	6.0 $^{+0.42}_{-0.38}$	27.20 \pm 0.30	3.01 \pm 0.08	9	Ly α (em)
gal2	198.78811	51.84276	0.5632 \pm 0.0004	0.550 $^{+0.123}_{-0.140}$	20.49 \pm 0.01	1.31 \pm 0.01	4	[OII], K, H, MgI, MgII
gal4	198.76596	51.85902	3.2269 \pm 0.002	3.44 $^{+0.09}_{-0.07}$	24.16 \pm 0.03	1.44 \pm 0.02	3	Ly α (abs), SiII, SiIV
gal11-a	198.76772	51.79678	2.2864 \pm 0.002	2.56 $^{+0.235}_{-0.235}$	22.86 \pm 0.01	2.18 \pm 0.05	4	Ly α (em), SiII, CIV
gal12	198.77770	51.79462	2.290 \pm 0.002	2.32 $^{+0.235}_{-0.235}$	25.32 \pm 0.08	2.14 \pm 0.05	4	Ly α (em), CIV, AlIII
gal13-b	198.77518	51.78871	1.035 \pm 0.001	1.05 $^{+0.108}_{-0.112}$	23.45 \pm 0.03	1.55 \pm 0.02	4	[OII]
gal16	198.79701	51.77606	0.3906 \pm 0.0005	—	—	1.10 \pm 0.01	4	K, H
gal17	198.79065	51.77097	1.236 \pm 0.0005	—	—	1.28 \pm 0.02	4	[OII]
gal18-b	198.78816	51.77364	0.5860 \pm 0.0005	—	—	1.19 \pm 0.01	4	[OII], MgII, K, H
gal19-a	198.77100	51.76841	0.2909 \pm 0.0005	—	—	1.01 \pm 0.01	4	K, H
gal19-b	198.77063	51.76935	0.3622 \pm 0.0005	—	—	1.06 \pm 0.01	4	[OII], K, H
gal1	198.78155	51.83971	0.1432 \pm 0.0005	—	—	—	4	[OII], H β , [OIII]
gal3	198.77735	51.85023	0.087 \pm 0.0005	—	—	—	4	[OII], K, H, H β , [OIII]
gal11-b	198.76774	51.79744	0.280 \pm 0.001	—	—	—	4	[OII], H β , [OIII]
gal13-a	198.77540	51.78808	0.1762 \pm 0.0005	—	—	—	4	K, H
gal14	198.78653	51.78574	0.1011 \pm 0.0003	—	—	—	4	[OII], H β , [OIII]
gal18-a	198.78753	51.77299	0.2705 \pm 0.0005	—	—	—	4	K, H
gal20	198.79633	51.76602	0.2766 \pm 0.0005	—	—	—	4	K, H
gal21	198.78704	51.76265	0.2781 \pm 0.0005	—	—	—	4	K, H
gal22-a	198.77246	51.75876	0.2410 \pm 0.0005	—	—	—	4	[OII], K, H
gal22-b	198.77236	51.76022	0.2766 \pm 0.0005	—	—	—	4	K, H
gal23	198.75441	51.86258	0.1765 \pm 0.0004	—	—	—	4	[OII], K, H, H β , [OIII]
gal24	198.75110	51.86508	0.2683 \pm 0.0005	—	—	—	4	K, H

Table 2. Overview of the sources included in the LRIS mask. From left to right: identification, astrometric position, spectroscopic redshift, photometric redshift estimate, ACS-F775W band photometry when available, magnification, redshift quality class (see Sect. 2.3), main spectroscopic features. The mentions (abs) and (em) refer to a Ly α line in absorption or in emission, respectively. The first part of the table corresponds to multiply-imaged system, the second part to background sources, the third part to cluster members and foreground sources.

ID	α (J2000.0)	δ (J2000.0)	z_{model}	z_{phot}	F775W	μ
New multiple images						
10.4	198.77173	51.81906	$z_{spec} = 2.627$	—	24.77 ± 0.08	4.15 ± 0.65
12.1	198.77456	51.829946	3.31 ± 0.16	$3.33^{+0.47}_{-0.32}$	26.68 ± 0.10	5.9 ± 0.4
12.2	198.76568	51.828658		$3.35^{+0.22}_{-0.31}$	24.47 ± 0.04	5.6 ± 0.8
12.3	198.75867	51.826482		$3.16^{+0.24}_{-0.53}$	26.33 ± 0.08	7.4 ± 0.3
13.1	198.78238	51.821204	0.839 ± 0.007	$1.15^{+0.13}_{-0.16}$	26.93 ± 0.11	3.9 ± 0.1
13.2	198.76796	51.818374		$0.68^{+0.46}_{-0.12}$	24.18 ± 0.04	9.3 ± 2.8
13.3	198.77204	51.814973		$1.13^{+0.08}_{-0.19}$	26.29 ± 0.08	7.3 ± 1.3
13.4	198.76692	51.815130		$1.07^{+0.19}_{-0.10}$	25.12 ± 0.05	11.9 ± 0.7
14.1	198.78662	51.820542	1.58 ± 0.02	—	25.55 ± 0.11	4.5 ± 0.1
14.2	198.76868	51.820191		—	25.40 ± 0.17	3.2 ± 1.4
14.3	198.76447	51.812192		—	26.33 ± 0.16	7.1 ± 0.2
14.4	198.77540	51.811945		—	26.30 ± 0.15	2.1 ± 0.2
Other multiple systems from L08						
2.2	198.77156	51.81174	$2.16^{+0.15}_{-0.09}$	$2.31^{+0.46}_{-0.38}$	25.29 ± 0.08	60 ± 10
2.3	198.76970	51.81186		$2.23^{+0.19}_{-0.66}$	26.15 ± 0.10	56 ± 8
8.1	198.77250	51.83045	$2.933^{+0.004}_{-0.077}$	$2.80^{+0.17}_{-0.09}$	24.95 ± 0.06	9.6 ± 1.6
8.2	198.76608	51.82949		$2.77^{+0.21}_{-0.11}$	23.06 ± 0.02	7.5 ± 0.7
8.3	198.75863	51.82740		$2.72^{+0.20}_{-0.12}$	25.07 ± 0.06	6.3 ± 0.2
9.1	198.77176	51.83030	$3.271^{+0.031}_{-0.124}$	—	26.68 ± 0.15	17.2 ± 3.2
9.2	198.76690	51.82957		$2.995^{+0.195}_{-0.378}$	25.32 ± 0.08	9.8 ± 1.7
9.3	198.75813	51.82708		$3.00^{+0.37}_{-0.60}$	26.92 ± 0.12	6.2 ± 0.1

Table 3. Location and redshift estimate of three new multiply-image systems, as well as the radial feature (10.4) associated with the giant arc (Systems 10 and 11). From left to right: identification, astrometric position, redshift estimate from the lensing model, photometric redshift estimate, magnification. We also report the same values for the three remaining systems from L08 (Systems 2, 8 and 9), used in the mass model but lacking spectroscopic redshifts. The redshift of this image 10.4 has a spectroscopic measurement and therefore is not a free parameter in the model. System 14 and image 9.1 are too faint to provide a reliable photometric redshift estimate.

Clump	(x)	(y)	e	θ	r (kpc)	α	c_{200}	σ_0 (kms $^{-1}$)	z_{model}
NFW	-0.79 ± 0.08	0.91 ± 0.08	0.230 ± 0.006	64.0 ± 0.3	$476.9^{+51.6}_{-42.8}$	$0.92^{+0.05}_{-0.04}$	$4.72^{+0.43}_{-0.45}$	—	—
cD	[0.0]	[0.0]	[0.19]	[52]	[25]			$355.7^{+10.3}_{-12.8}$	—
Galaxy 852	[19.0]	[54.0]	[0.11]	[65.5]	98.7 ± 1.8			320.9 ± 3.5	—
L $_{*}$ elliptical galaxy					$68.8^{+0.2}_{-1.8}$			202^{+2}_{-3}	—

Table 4. Best fit parameters used to model the mass distribution. The positions (x) and (y) are in arcsecs relative to the central galaxy (R.A.=13:15:05.276, Decl.=+51:49:02.85) and oriented in WCS (North is up, East is left). Orientations θ are measured in degrees and ellipticities (e) are given as $1 - b/a$, where a and b are the semi-major and semi-minor axis of the ellipse, respectively. Values in brackets were not optimized by the model. The radius (r) refers to the scale radius r_s in the case of the gNFW profile, and the r_{cut} radius in the case of the PIEMD profile (see L08 for details).